SOLAR CELLS

Thermodynamically stabilized β-$CsPbI_3$–based perovskite solar cells with efficiencies >18%

Yong Wang[1], M. Ibrahim Dar[2]*, Luis K. Ono[3], Taiyang Zhang[1], Miao Kan[1], Yawen Li[4], Lijun Zhang[4], Xingtao Wang[1], Yingguo Yang[5], Xingyu Gao[5], Yabing Qi[3]*, Michael Grätzel[2]*, Yixin Zhao[1,6]*

Although β-$CsPbI_3$ has a bandgap favorable for application in tandem solar cells, depositing and stabilizing β-$CsPbI_3$ experimentally has remained a challenge. We obtained highly crystalline β-$CsPbI_3$ films with an extended spectral response and enhanced phase stability. Synchrotron-based x-ray scattering revealed the presence of highly oriented β-$CsPbI_3$ grains, and sensitive elemental analyses—including inductively coupled plasma mass spectrometry and time-of-flight secondary ion mass spectrometry—confirmed their all-inorganic composition. We further mitigated the effects of cracks and pinholes in the perovskite layer by surface treating with choline iodide, which increased the charge-carrier lifetime and improved the energy-level alignment between the β-$CsPbI_3$ absorber layer and carrier-selective contacts. The perovskite solar cells made from the treated material have highly reproducible and stable efficiencies reaching 18.4% under 45 ± 5°C ambient conditions.

The state-of-the-art power-conversion efficiencies (PCEs) reported for inorganic perovskite solar cells (PSCs), typically ~15%, are substantially lower than those of the hybrid organic-inorganic metal halide PSCs (as high as 24.2%), primarily because all-inorganic perovskites have larger bandgaps and less favorable photophysical properties (*1*–*3*). Cesium lead iodide ($CsPbI_3$) has the most promising bandgap for applications as two-level tandem solar cells in combination with silicon (*4*, *5*), but the small size of Cs^+ gives rise to the unideal tolerance factor that makes it difficult to stabilize the $CsPbI_3$ perovskite phase under ambient conditions (*6*–*9*). Theoretical calculations predict that the tetragonal (β-phase) polymorph of $CsPbI_3$ can be crystallized at lower temperatures and would have a more stable perovskite structure than the cubic α-phase (*10*–*13*), but experimentally it has been challenging to deposit and stabilize β-$CsPbI_3$ for high-efficiency PSCs (*14*).

[1]School of Environmental Science and Engineering, Frontiers Science Center for Transformative Molecules, Shanghai Jiao Tong University, Shanghai 200240, China. [2]Laboratory of Photonics and Interfaces, Institute of Chemical Sciences and Engineering, Ecole Polytechnique Federale de Lausanne, CH-1015 Lausanne, Switzerland. [3]Energy Materials and Surface Sciences Unit (EMSSU), Okinawa Institute of Science and Technology Graduate University (OIST), Okinawa 904-0495, Japan. [4]State Key Laboratory of Superhard Materials, Key Laboratory of Automobile Materials of MOE, and School of Materials Science and Engineering, Jilin University, Changchun 130012, China. [5]Shanghai Synchrotron Radiation Facility (SSRF), Zhangjiang Lab, Shanghai Advanced Research Institute, Chinese Academy of Sciences, Shanghai 201204, China. [6]Shanghai Institute of Pollution Control and Ecological Security, Shanghai 200092, China.
*Corresponding author. Email: yixin.zhao@sjtu.edu.cn (Y.Z.); michael.graetzel@epfl.ch (M.G.); yabing.qi@oist.jp (Y.Q.); ibrahim.dar@epfl.ch (M.I.D.)

We have grown highly stable β-$CsPbI_3$ perovskite films with extended ultraviolet-visible (UV-vis) absorbance and fabricated PSCs with 15.1% PCE. Furthermore, we developed a crack-filling interface engineering method using choline iodine (CHI), which not only passivated the surface trap states of perovskite but also led to better matching of the energy levels at the interfaces between the β-$CsPbI_3$ perovskite and the TiO_2 electron-transport layer (ETL), as well as with the spiro-OMeTAD {2,2′,7,7′-tetrakis[*N*,*N*-bis(*p*-methoxyphenyl)amino]-9,9′-spirobifluorene} hole-transport layer (HTL). With this approach, the efficiency of β-$CsPbI_3$–based PSCs improved to 18.4% with high stability and reproducibility.

To mitigate the challenge of obtaining the $CsPbI_3$ perovskite phase through a conventional solvent engineering method from PbI_2 and CsI precursors (fig. S1), we spin-coated a precursor solution containing a stoichiometric mixture of $PbI_2{\cdot}x$DMAI (x = 1.1 to 1.2; DMAI, dimethylammonium iodide) and CsI onto a compact TiO_2 layer (figs. S2 to S5). After annealing at 210°C for 5 min, the $CsPbI_3$ films showed an absorbance edge ~736 nm (Fig. 1A) and a bandgap of 1.68 eV as determined from a Tauc plot (fig. S2), substantially redshifted relative to the ~1.73 eV value previously reported for $CsPbI_3$ films (*4*).

To rule out the incorporation of any organic A-site cations that could have caused this redshift, we used thermogravimetric analysis and nuclear magnetic resonance (NMR) spectroscopy (figs. S3 and S4). Both techniques establish that an optimized annealing process at ~210°C for 5 min was sufficient to remove all organic species. This conclusion was further supported by absorption and x-ray diffraction (XRD) data recorded for the samples annealed at ~210°C for different periods of time (fig. S5). We also evaluated the composition of the perovskite films by using inductively coupled plasma mass spectrometry (ICP-MS) and time-of-flight secondary ion mass spectrometry (TOF-SIMs) (table S1 and fig. S6). These methods confirmed that the perovskite films are exclusively inorganic. In contrast, ICP-MS and TOF-SIMs revealed a deficiency of Cs^+ and the presence of organic A-site cations (dimethylammonium) in perovskite films that were annealed at lower temperatures (100° to 110°C) (*15*).

The desired redshift is associated with the specific phase of $CsPbI_3$ (*13*). To determine the crystal structure of the perovskite films, we used x-ray scattering (XRD) techniques, including synchrotron-based grazing incidence wide-angle x-ray scattering (GIWAXS). We indexed the XRD patterns to β-$CsPbI_3$ (Fig. 1B and fig. S7), a phase of $CsPbI_3$ previously observed only above 230°C. Although the XRD pattern measured at room temperature will not be identical to the standard XRD pattern obtained at higher temperature owing to the lattice thermal expansion, the basic features of the patterns should be very similar, and the in situ temperature-dependent GIWAXS pattern of our β-$CsPbI_3$ shows only small variation between 30° and 250°C (figs. S8 and S9). Relatively intense (110) and (220) reflections further indicate a preferred (110) orientation of the β-$CsPbI_3$ grains. Powder samples obtained from scratching the $CsPbI_3$ films revealed peak splitting at 28° to 29° for 2θ (Fig. 1B), as expected for the tetragonal β-$CsPbI_3$ phase. The pattern was markedly different from those of α- and γ-$CsPbI_3$ systems (fig. S10). Notably, most of the previously reported XRD patterns that have been incorrectly indexed to the α-$CsPbI_3$ phase actually correspond to γ-$CsPbI_3$, in accordance with the large bandgap of ~1.73 eV of the latter system.

The GIWAXS data (Fig. 1C) not only established the formation of β-$CsPbI_3$ but also revealed peak splitting of the tetragonal crystallites in the (220) class of reflections. Radially integrated intensity plots (fig. S11) along the ring at $\mathbf{q}$ = 10 nm^{-1} [scattering vector $\mathbf{q} = 4\pi\sin(\theta)/\lambda$ (λ, wavelength)] at azimuthal angles of 90° further indicate a strong preferred (110) orientation of the β-$CsPbI_3$ grains. First-principles modeling that used theoretically optimized structures (fig. S12) rationalized the lower bandgap of tetragonal β-$CsPbI_3$ relative to orthorhombic γ-$CsPbI_3$ in terms of the degree of distortion away from the ideal cubic structure.

Scanning electron microscopy (SEM) revealed that the 350- to 400-nm-thick β-$CsPbI_3$ perovskite films are composed of submicrometer-sized grains (Fig. 1D), comparable to the film thickness, which enables efficient charge extraction (*16*). Previous studies on $CsPbI_3$ reported that smaller grain size can improve perovskite phase stability and also suggested poor stability of the β-$CsPbI_3$ phase at low temperature, so we further evaluated the thermal stability of highly crystalline β-$CsPbI_3$ (*7*, *14*). The β-$CsPbI_3$ films, without any additional treatment, retained their color and phase even after annealing at 70°C for

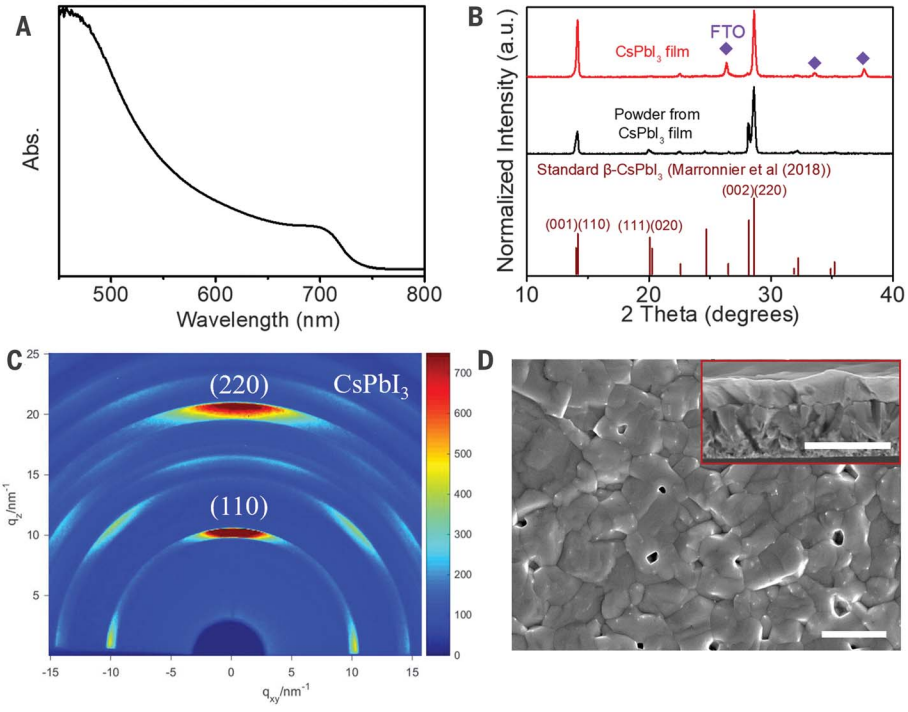

Fig. 1. Spectroscopic, structural, and morphological characterization of β-$CsPbI_3$ thin films. (**A**) UV-vis spectrum. (**B**) XRD patterns acquired from a $CsPbI_3$ thin film and powders scratched from the films. Brown lines indicate the standard β-$CsPbI_3$ XRD pattern calculated for Cu Kα1 radiation for the tetragonal perovskite structure determined by Marronnier *et al*. at 518 K (*13*). a.u., arbitrary units. (**C**) GIWAXS data from β-$CsPbI_3$ films. (**D**) Top-surface SEM image of β-$CsPbI_3$. The inset presents the cross-sectional morphology of the β-$CsPbI_3$ perovskite thin film. Scale bars, 1 μm.

>200 hours in the nitrogen glovebox (fig. S13). Compared with $MAPbI_3$, the β-$CsPbI_3$ films also exhibited better phase stability (fig. S14). However, they turned into the undesired yellow phase when exposed to 85 ± 5% relative humidity (RH) at 30°C after several minutes (fig. S15).

We fabricated planar PSCs with the configuration of FTO/c-TiO_2/perovskite/spiro-OMeTAD/Ag, where FTO is fluorine-doped tin oxide and c-TiO_2 is compact TiO_2. Under standard 1.5G illumination, the best β-$CsPbI_3$ PSC showed a PCE of 15.1% with a short-circuit photocurrent density (J_{sc}) = 20.03 mA cm^{-2}, an open-circuit photovoltage (V_{oc}) = 1.05 V, and a fill factor (*FF*) = 0.72 (fig. S16). This state-of-the-art efficiency for an all-inorganic perovskite is still substantially lower than the PCEs reported for the PSCs fabricated from organic-inorganic hybrid perovskites with bandgaps near that of β-$CsPbI_3$. The large hysteresis presents an additional caveat. The low efficiency of β-$CsPbI_3$ PSCs is mainly related to the modest V_{oc} and *FF* (fig. S16). Previous studies have suggested that the reduced V_{oc} and *FF* could be associated with the poor band alignment and nonradiative carrier recombination at the surface defects (*17*–*19*).

To further enhance the PCE of β-$CsPbI_3$ PSCs, we used the cracks present on the perovskite films to passivate the grains and simultaneously improve the alignment between perovskite and ETL layer. We selected CHI, which has been previously used to passivate hybrid perovskite films (*20*), and we then spin-coated CHI from isopropanol (IPA) solution (1 mg ml^{-1}) onto β-$CsPbI_3$ thin films (hereafter, 1 mg ml^{-1} CHI-treated β-$CsPbI_3$ is referred to as CHI-$CsPbI_3$) (Fig. 2A). The SEM images (fig. S17) and carbon distribution profiles across the perovskite layer (Fig. 2, B and C, and fig. S18) indicate that the CHI penetrates into the bulk of the $CsPbI_3$ thin films, possibly through the pinholes and cracks. This CHI treatment improved the energy-level alignment of the conduction band minimum between β-$CsPbI_3$ and TiO_2 by 120 meV (Fig. 2, D to F, and fig. S19). Furthermore, the CHI treatment led to improved energy-level alignment at both the β-$CsPbI_3$/ETL interface and the β-$CsPbI_3$/HTL interface.

The CHI treatment had a negligible effect on the absorption features, as the absorbance edge of CHI-$CsPbI_3$ films is still ~736 nm (~1.68 eV) (Fig. 3A). Likewise, the XRD patterns of pristine and CHI-$CsPbI_3$ perovskite films (Figs. 1B and 3B) were almost identical. The comparison of Fig. 3C and fig. S16 shows that the CHI homogeneously distributes on the surface of film and the pinhole locations are filled with CHI. The NMR-based quantitative analysis revealed that the CHI is only ~1 weight % of the CHI-$CsPbI_3$ film (fig. S20). The XRD patterns, UV-vis absorption spectra, and surface morphology of the β-$CsPbI_3$ perovskite thin films treated with the different concentrations of CHI solution are presented in fig. S21.

The high-resolution cross-sectional SEM images (fig. S22A) revealed continuous monolithic-type grains extending vertically across the entire $CsPbI_3$ film thickness but also some pinholes in the bulk of the films. The subsequent CHI spin-coating treatment only filled these pinholes and cracks and did not lead to substantial disruptions in the structure, morphology, and absorption properties of the β-$CsPbI_3$ films (fig. S22B). To exclude the effect of the IPA solvent, the $CsPbI_3$ films treated only with IPA were further characterized by SEM (fig. S23), which showed a morphology similar to that of the $CsPbI_3$ films.

We also used time-resolved photoluminescence (TRPL) spectroscopy to investigate the impact of CHI treatment on the excitonic quality of perovskite films. The charge carriers are relatively long-lasting in the case of CHI-$CsPbI_3$ films (Fig. 3D), which is likely the result of a reduction in nonradiative recombination by trap passivation, which improved the overall charge-carrier dynamics. We calculated Urbach energies (fig. S24) (*21*, *22*) of 15.9 meV for $CsPbI_3$ and 14.4 meV for CHI-$CsPbI_3$. The Urbach energy for the CHI-$CsPbI_3$ should correspond to a lower density of trap states, consistent with the TRPL result.

X-ray photoelectron spectroscopy (XPS) measurements were conducted to further explore the effect of CHI treatment on the chemical composition of perovskite films. All core-level peaks were assigned to Cs, Pb, I, C, N, and O (Fig. 3E and fig. S25). The absence of a Ti 2p peak confirmed the uniformity of coverage of the perovskite film on top of the TiO_2 substrate. No binding energy shifts or additional peaks were observed for Cs 3d, Pb 4f, or I 3d, establishing that the CHI treatment improves the interfacial properties without changing the chemical nature of the all-inorganic $CsPbI_3$ perovskite photoactive layer (fig. S25). A small O 1s peak was also observed for the pristine β-$CsPbI_3$ sample (Fig. 3E), possibly a result of a small amount of oxygen adsorbed on the sample surface and/or diffused into the sample during preparation in dry-O_2 conditions (*23*). Furthermore, energy-dispersive x-ray spectroscopy (EDX) elemental mapping (Fig. 3F and fig. S26) shows a uniform distribution of N and O on the surface of CHI-$CsPbI_3$. More importantly, the CHI-$CsPbI_3$

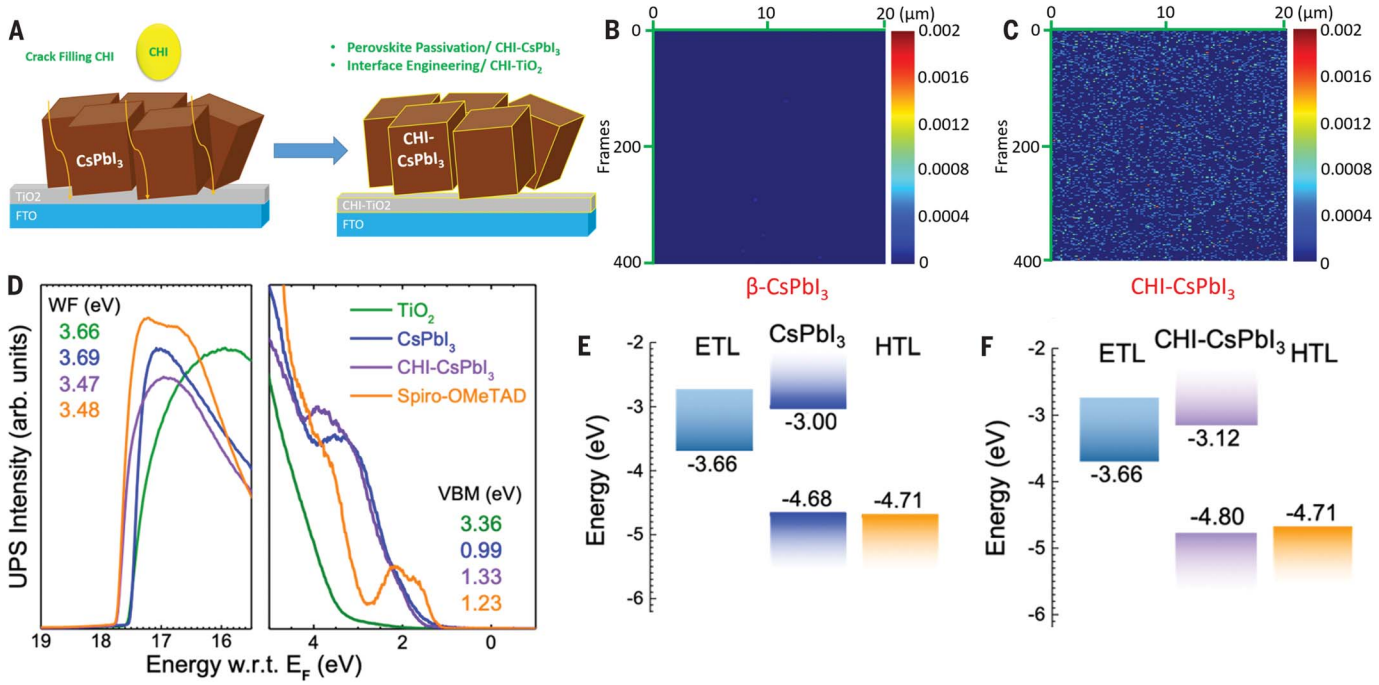

Fig. 2. Effect of crack-filling interface engineering treatment on the energy-level alignment. (**A**) Schematic illustration of crack-filling interface engineering. (**B** and **C**) Comparison of cross-sectional carbon element analysis for the (B) β-$CsPbI_3$ and (C) CHI-$CsPbI_3$ films measured by TOF-SIMS. (**D**) Ultraviolet photoelectron spectroscopy (UPS) spectra (using the He-I line with photon energy of 21.22 eV) corresponding to the secondary electron onset region (WF, work function) and valence band region (VBM, valence band minimum) of the as-prepared $CsPbI_3$, CHI-$CsPbI_3$ perovskite films, TiO_2 (ETL), and the highest occupied molecular orbital of the spiro-OMeTAD (HTL) with respect to the Fermi energy (w.r.t. E_F). VBM onsets for perovskites were determined from semi-log plots (fig. S19). (**E** and **F**) Corresponding energy diagram of (E) the $CsPbI_3$ film and (F) the CHI-$CsPbI_3$ film together with the TiO_2 ETL and spiro-OMeTAD HTL that constitute the solar cell architecture.

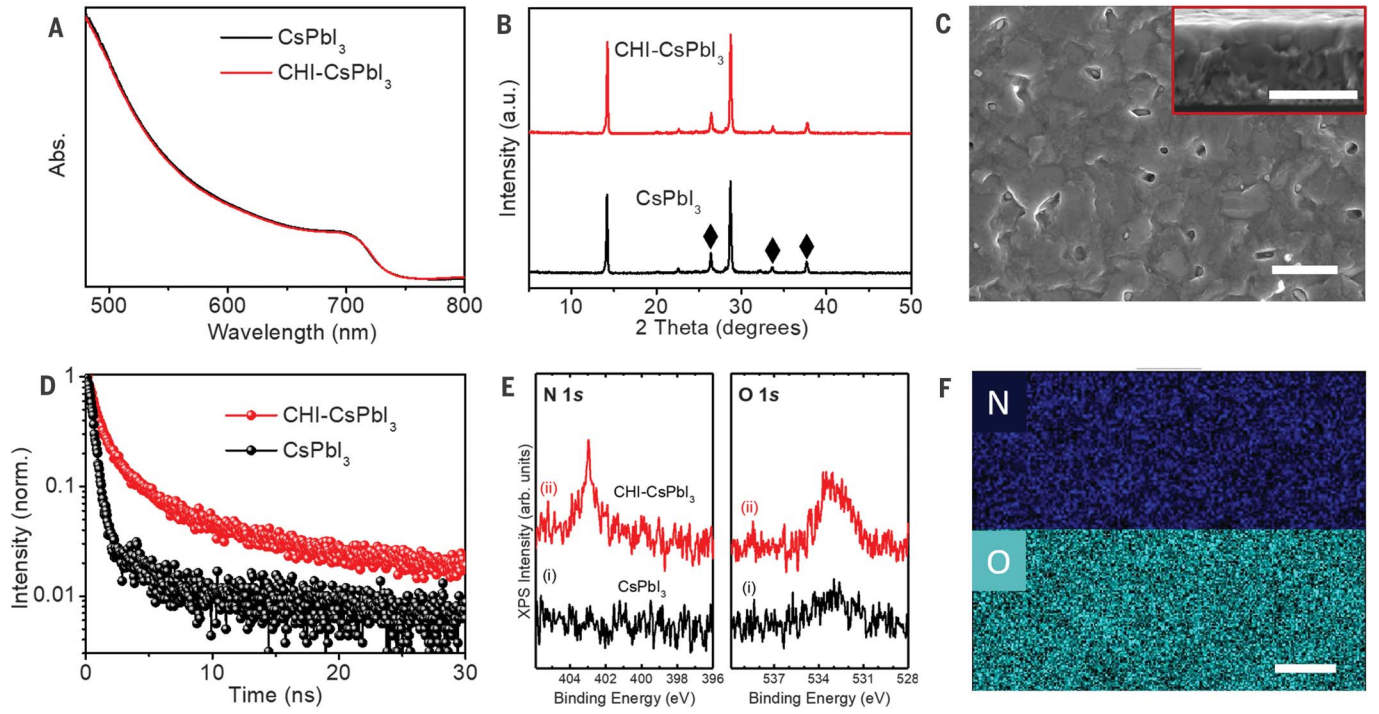

Fig. 3. Effects of CHI treatment on the spectroscopy and structure of β-$CsPbI_3$ perovskite thin films. (**A**) UV-vis spectra, (**B**) XRD patterns, and (**C**) top-surface SEM image of CHI-$CsPbI_3$ perovskite thin films. Diamond symbols represent the FTO substrate. The inset in (C) shows the cross-section morphology of the CHI-$CsPbI_3$ perovskite thin films. Abs., absorbance. (**D**) TRPL decay curves of $CsPbI_3$ and CHI-$CsPbI_3$ thin films. norm., normalized. (**E**) XPS (Al-K = 1486.6 eV) N 1s and O 1s core-level spectra for the CHI-$CsPbI_3$ sample. (**F**) EDX top-view element mapping of N and O distribution on the surface of CHI-$CsPbI_3$ perovskite thin films. Scale bars, 1 μm.

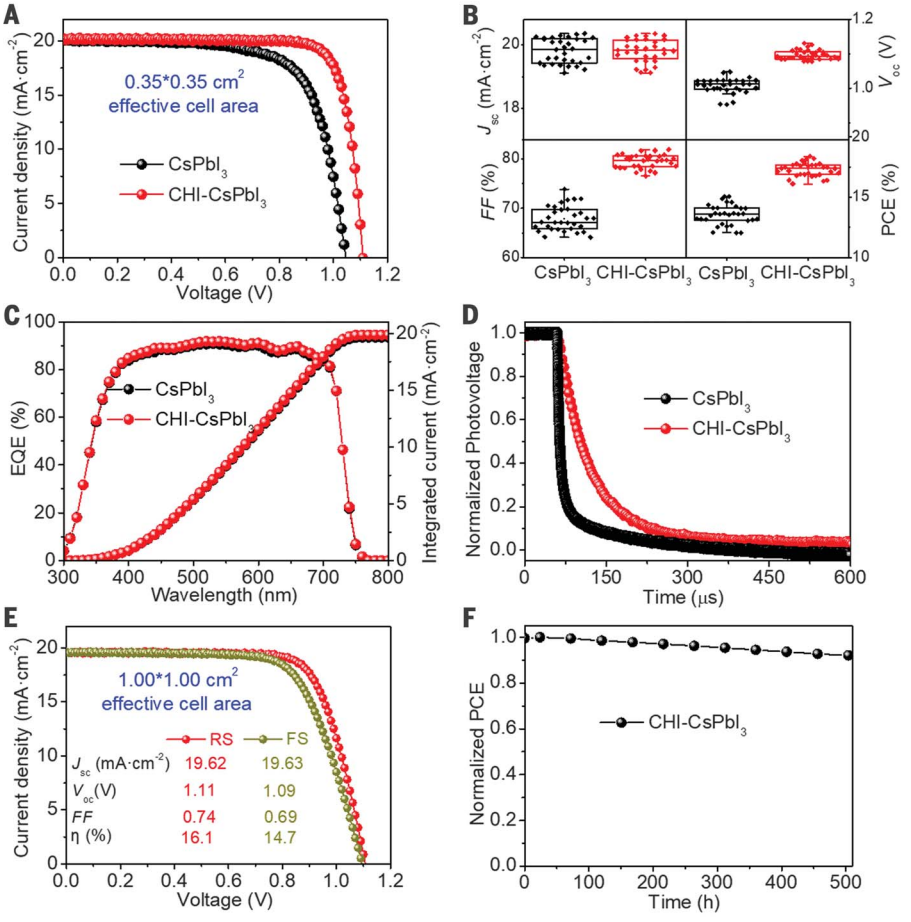

Fig. 4. Photovoltaic and device characterization. (**A**) *J-V* characteristics of PSCs based on $CsPbI_3$ and CHI-$CsPbI_3$ with 0.1-cm^2 effective cell area under simulated AM 1.5G solar illumination of 100 mW cm^{-2} in reverse scan. (**B**) Corresponding PV metrics (0.1-cm^2 effective cell area; 32 devices). All *J-V* curves were measured at ~45 ± 5°C under full-sun illumination. (**C**) EQE spectrum together with the integrated J_{sc} for the $CsPbI_3$- and CHI-$CsPbI_3$–based PSCs. (**D**) TPV of $CsPbI_3$- and CHI-$CsPbI_3$–based PSCs. (**E**) *J-V* characteristics of PSCs based on CHI-$CsPbI_3$ with 1-cm^2 effective cell area under simulated AM 1.5G solar illumination of 100 mW cm^{-2} in forward and reverse scans. J_{sc}, short-circuit photocurrent density; V_{oc}, open-circuit voltage; *FF*, fill factor; η, PCE. (**F**) Photostability of the unencapsulated CHI-$CsPbI_3$ PSC devices under continuous white light LED (light-emitting diode) illumination (100 mW cm^{-2}) at their MPP in a N_2 glovebox.

perovskite thin films exhibited greater resistance toward humidity and also showed good thermal stability (figs. S27 and S28).

We compared the *J-V* characteristics of the best-performing PSCs based on CHI-$CsPbI_3$ and β-$CsPbI_3$ perovskite films (Fig. 4A). Although the J_{sc} remained unaffected, the CHI-$CsPbI_3$–based PSC showed better V_{oc} (1.11 versus 1.05 V) and *FF* (0.82 versus 0.72), improving the overall PCE from 15.1 to 18.4% (Fig. 4, B and C). We also obtained a certified PCE of 18.3% for CHI-$CsPbI_3$–based PSC (fig. S29). Additionally, we compared the PV parameters of $CsPbI_3$- and CHI-$CsPbI_3$–based PSCs (Fig. 4B). For the latter, the V_{oc} and *FF* are substantially enhanced. We attributed this improvement to better energy-level alignment and desired charge-carrier dynamics. All *J-V* curves were measured at ~45 ± 5°C under full-sun illumination (100 mW cm^{-2}). Figure S30 shows that the efficiency drops marginally at ~60°C. Furthermore, the CHI-$CsPbI_3$–based PSCs exhibit a smaller hysteresis, resulting in a stabilized output power of 17.8% (figs. S31 and S32). The external quantum efficiency (EQE) of CHI-$CsPbI_3$–based PSCs (Fig. 4C) is >90% for wavelengths between 500 and 600 nm. The integrated J_{sc} of 19.85 mA cm^{-2} calculated from the EQE is comparable to the value estimated for the pure $CsPbI_3$ device (19.71 mA cm^{-2}), in agreement with the *J-V* characteristics. Furthermore, the photovoltaic (PV) performance of $CsPbI_3$ treated with 0.5 or 2 mg ml^{-1} CHI also exhibited ~17% PCE, which was much higher than that of pure β-$CsPbI_3$–based devices (fig. S33).

We further investigated the charge-transport properties of CHI-treated PSCs by using transient photocurrent decay (TPC) and transient photovoltage decay (TPV) measurements. Similar TPC responses (fig. S34) suggest that the CHI treatment had minimal influence on the charge transport or charge collection efficiency, in agreement with J_{sc} and EQE results. In contrast, the TPV revealed that CHI treatment increased charge-carrier lifetime (Fig. 4D), indicating a decrease in the undesired charge-carrier recombination (*24*, *25*).

We fabricated large-area PSCs based on CHI-$CsPbI_3$ thin films. The best CHI-$CsPbI_3$ devices, fabricated on 2.5 cm–by–2.5 cm substrates with an effective cell area of 1 cm^2 (Fig. 4E), display a PCE of 16.1% with J_{sc} of 19.62 mA cm^{-2}, V_{oc} of 1.11 V, and *FF* of 0.74 under reverse scan conditions. The PV metrics (fig. S35 and table S2) show an average efficiency as high as 15.2%. These large-area devices also show small hysteresis (Fig. 4E) and high EQE and stabilized PCE (figs. S36 and S37). Furthermore, the CHI-$CsPbI_3$–based PSCs stored in a N_2 glovebox retain 92% of their initial PCE after 500 hours of continuous illumination at the maximum power point (MPP) (Fig. 4F). The CHI-$CsPbI_3$–based PSCs stored in a dark, dry box (RH < 10%) with oxygen exhibit no PV performance decay (fig. S38A). The encapsulated device shows excellent ambient stability (fig. S38B) and retains 95% of its initial PCE in air after 240 hours of continuous illumination at the MPP (fig. S38, C and D).

REFERENCE AND NOTES

1. A. Swarnkar *et al.*, *Science* **354**, 92–95 (2016).
2. P. Wang *et al.*, *Nat. Commun.* **9**, 2225 (2018).
3. B. Zhao *et al.*, *J. Am. Chem. Soc.* **140**, 11716–11725 (2018).
4. G. E. Eperon *et al.*, *J. Mater. Chem. A* **3**, 19688–19695 (2015).
5. E. M. Sanehira *et al.*, *Sci. Adv.* **3**, eaao4204 (2017).
6. S. Dastidar *et al.*, *Nano Lett.* **16**, 3563–3570 (2016).
7. T. Zhang *et al.*, *Sci. Adv.* **3**, e1700841 (2017).
8. B. Li *et al.*, *Nat. Commun.* **9**, 1076 (2018).
9. A. K. Jena, A. Kulkarni, Y. Sanehira, M. Ikegami, T. Miyasaka, *Chem. Mater.* **30**, 6668–6674 (2018).
10. R. J. Sutton *et al.*, *ACS Energy Lett.* **3**, 1787–1794 (2018).
11. C. C. Stoumpos, M. G. Kanatzidis, *Acc. Chem. Res.* **48**, 2791–2802 (2015).
12. C. C. Stoumpos, C. D. Malliakas, M. G. Kanatzidis, *Inorg. Chem.* **52**, 9019–9038 (2013).
13. A. Marronnier *et al.*, *ACS Nano* **12**, 3477–3486 (2018).
14. Y. Fu *et al.*, *Chem. Mater.* **29**, 8385–8394 (2017).
15. W. Ke, I. Spanopoulos, C. C. Stoumpos, M. G. Kanatzidis, *Nat. Commun.* **9**, 4785 (2018).
16. N. J. Jeon *et al.*, *Nat. Energy* **3**, 682–689 (2018).
17. N. Arora *et al.*, *ACS Energy Lett.* **1**, 107–112 (2016).
18. H. Chen *et al.*, *Adv. Energy Mater.* **7**, 1700012 (2017).
19. Y. Shao, Y. Yuan, J. Huang, *Nat. Energy* **1**, 15001 (2016).
20. X. Zheng *et al.*, *Nat. Energy* **2**, 17102 (2017).
21. P. Löper *et al.*, *J. Phys. Chem. Lett.* **6**, 66–71 (2015).
22. W. Zhang *et al.*, *Nat. Commun.* **6**, 10030 (2015).
23. L. K. Ono *et al.*, *J. Phys. Chem. Lett.* **5**, 1374–1379 (2014).
24. H. Tan *et al.*, *Science* **355**, 722–726 (2017).
25. T. Leijtens *et al.*, *Energy Environ. Sci.* **9**, 3472–3481 (2016).

ACKNOWLEDGMENTS

We thank the Instrumental Analysis Center (School of Environmental Science and Engineering and Shanghai Jiao Tong University) for assistance with material characterization tests. We also thank the National Institute of Metrology (China) for authentication tests. **Funding:** The work performed at Shanghai Jiao Tong University was supported by the NSFC (grants

21777096 and 51861145101), a Huoyingdong grant (151046), a Shanghai Shuguang grant (17SG11), and the China Postdoctoral Science Foundation (2017M621466). The work performed at the Okinawa Institute of Science and Technology Graduate University was supported by funding from the Energy Materials and Surface Sciences Unit of the Okinawa Institute of Science and Technology Graduate University, the OIST R&D Cluster Research Program, the OIST Proof of Concept (POC) Program, and a JSPS KAKENHI grant (JP18K05266). The work performed at Jilin University was supported by the National Natural Science Foundation of China (grants 61722403 and 11674121). M.I.D acknowledges financial support from the Swiss National Science Foundation under the project number P300P2_174471. Y.Y. and X.G. acknowledge the support of the National Key Research and Development Program of China (2017YFA0403400). Calculations were performed at the High Performance Computing Center of Jilin University. **Authors contributions:** Y.Z., Y.Q., and M.G. designed and directed the study. Y.W. and T.Z. conceived and performed the device fabrication work. Y.L. and L.Z. performed the first-principles calculations and analyzed the results. Y.W., M.I.D., L.K.O., T.Z., M.K., X.W., Y.Y., X.G., Y.L., L.Z., Y.Q., M.G., and Y.Z. participated in characterization and data analysis. All authors contributed to the discussions. Y.W., Y.Z., M.I.D., Y.Q., and M.G. wrote the manuscript with input from all authors. All authors reviewed the paper. **Competing interests:** None declared. **Data and materials availability:** The data that support the findings of this study are available from the corresponding author upon request. All other data needed to evaluate the conclusions in the paper are present in the paper or the supplementary materials.

SUPPLEMENTARY MATERIALS

29 October 2018; resubmitted 16 May 2019
Accepted 9 July 2019
10.1126/science.aav8680

Science

Thermodynamically stabilized β-$CsPbI_3$–based perovskite solar cells with efficiencies >18%

Yong Wang, M. Ibrahim Dar, Luis K. Ono, Taiyang Zhang, Miao Kan, Yawen Li, Lijun Zhang, Xingtao Wang, Yingguo Yang, Xingyu Gao, Yabing Qi, Michael Grätzel and Yixin Zhao

Science **365** (6453), 591-595.
DOI: 10.1126/science.aav8680

Orthorhombic phases for perovskite solar cells

The power conversion efficiencies (PCEs) of all-inorganic perovskites are lower than those of materials with organic cations. This is in part because these materials have larger bandgaps. The cubic crystal phases of these materials also exhibit poor stability. Wang *et al.* synthesized the orthorhombic β-phase of $CsPbI_3$ from $HPbI_3$ and CsI. The material exhibited higher stability and a more favorable bandgap, which allowed for PCEs of 15%. Passivation of the surface trap state with choline iodide boosted PCEs to 18%.

Science, this issue p. 591